Experimental Mechanics
DOI 10.1007/s11340-008-9178-5

Large Deformation of Nitinol Under Shear Dominant Loading

S. Daly · D. Rittel · K. Bhattacharya · G. Ravichandran

Received: 7 January 2008 / Accepted: 25 August 2008

Abstract Full-field quantitative strain maps of phase transformation and plasticity in Nitinol under large shear-dominated deformation are presented. To achieve a shear-dominated deformation mode with relatively uniform stresses and strains, a shear compression specimen (SCS) geometry was utilized. Shear deformation appears to impede the development of the strain localization during phase transformation that is seen in uniaxial testing. The shear-dominant deformation of Nitinol in the plastic regime exhibits low hardening and results in the development of significant strain inhomogeneity.

Keywords Shape-memory alloy · Nitinol · Shear · Digital image correlation

Introduction

Shape-Memory Alloys (SMAs) have the ability to return to a previously defined shape when heated past a set transformation temperature following deformation. Many SMAs also display superelastic or pseudoelastic behavior, where large deformation (up to 8%) can be recovered upon unloading. The deformation is recovered in the shape-memory effect and in superelasticity because these are accommodated by martensitic phase transformation and transformation twinning/detwinning rather than by crystallographic slip [1, 2]. These materials undergo a martensitic phase transformation from a high temperature-high symmetry austenitic state to a low temperature-low symmetry martensitic state. The change of symmetry gives rise to multiple variants of martensite which can form transformation twins. Superelastic behavior arises when the material is deformed at a temperature that exceeds the transformation temperature. The stress-induced austenite to martensite transformation gives rise to the deformation on loading. However, the martensite is unstable at this temperature and it transforms back to the austenite upon unloading, thereby recovering the deformation. The mechanism of transformation is reasonably well understood in single crystals (see for example [3] and the references therein), but incompletely understood in polycrystals.

The shape memory effect and pseudoelasticity make SMAs, and in particular Nickel–Titanium (Nitinol), attractive for a variety of applications. The effect of large shear-dominated deformation in SMAs and the resulting phase transformation and plasticity is relevant in many of these applications, including ductile fracture, the micromechanics of void growth and coalescence, embedded SMAs, and numerous biomedical applications including stents, vena-cava filters, braided catheters, surgical tools and others (see for example [4] and the references therein). However, it is remarkably difficult to achieve a state of pure shear in most specimen geometries. Rittel et al. [5] recently developed a simple specimen geometry for the large strain constitutive testing of materials over a wide range of strain rates. Rittel et al. demonstrated that the dominant deformation mode in

S. Daly (✉, SEM Member)
Department of Mechanical Engineering, University of Michigan,
Ann Arbor, MI 48105, USA
e-mail: samdaly@umich.edu

D. Rittel (SEM Member)
Department of Mechanical Engineering, Technion,
Israel Institute of Technology,
32000 Haifa, Israel

K. Bhattacharya · G. Ravichandran (SEM Member)
Division of Engineering and Applied Science,
California Institute of Technology,
Pasadena, CA 91125, USA

the gage section of this 'shear compression specimen' (SCS) is shear, and thus large deformations can be achieved for ductile specimens without the usual plastic instabilities or barreling inherent to uniaxial testing. Numerical analysis on the SCS geometry confirmed that the stresses and strains in the test gage section are relatively uniform and that the resulting macroscopic stress–strain relationships are fairly simple. For this reason, and also for the inherent simplicity of the SCS and its ease of use during testing, this specimen geometry is well suited for the study of shear localization and large deformation in Nitinol. A detailed description of the SCS geometry and validation can be found in "Material and Specimen" and in references [5, 6].

Because the SCS geometry is simple and well-characterized, with predominately uniform shear in the gage section, it can be effectively used to learn about the deformation of polycrystalline Nitinol under large shear. Although large-scale shear is a common and an important occurrence, very little is currently known about the behavior of Nitinol under this mode of deformation. This is particularly true for the behavior of Nitinol beyond the superelastic regime. The plastic deformation of Nitinol is not well-characterized, and the constitutive data gathered in the experiments presented in this paper are meant to shed light on the behavior of Nitinol in this regime. The purpose of the following experiments is to obtain quantitative, full-field information detailing the behavioral response of Nitinol to large-scale shear dominant deformation. This is accomplished through the simultaneous application of large shear via the SCS geometry and the use of digital image correlation (DIC).

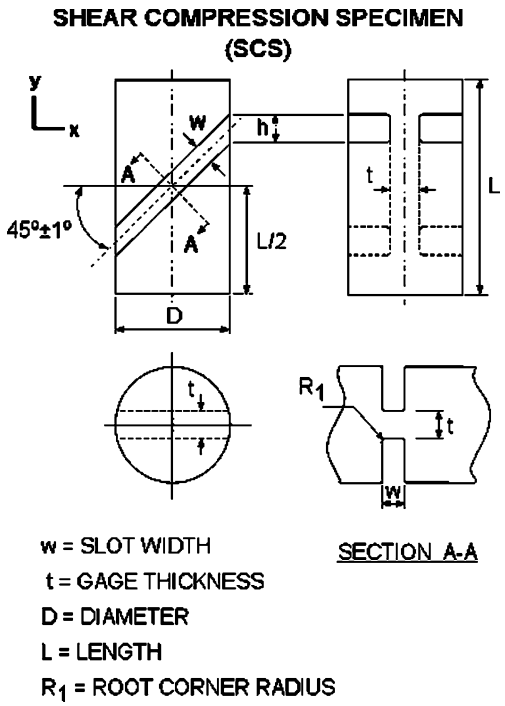

Fig. 1 Geometry of the shear compression specimens (SCS). The *x*–*y* coordinates are the Cartesian (laboratory) frame of reference

Methods

Material and Specimen

Samples were cut from an austenitic Nitinol bar (Nitinol Devices and Components, Fremont, CA) with a nominal diameter of 7.5 mm. The austenite finish temperature (A_f) of the bar was 7.77°C (280.77 K). Since the ambient (room) temperature during the tests (nominally 21°C) was significantly higher than the A_f temperature of the bar, the specimens were fully austenitic at the beginning of the test and the stress-induced martensite transformation occurred upon loading at room temperature.

The tests were performed on shear compression specimens (SCS), which are especially suitable for large shear dominated deformation [5]. The shape and dimensions of the SCS are shown in Fig. 1, where, L=15 mm, w=1.5 mm, D=7.5 mm, t=1.87 mm and R_1=0.15 mm. The specimen geometry consists of a cylinder with two diametrically opposed slots machined at 45° with respect to the longitudinal axis. These two slots form the gage section of the test sample. Upon longitudinal compression of the cylinder, the gage section is subjected to a dominant state of shear deformation. Although the stress (strain) state in the gage is three-dimensional rather than simple shear, the stresses and strains have been shown to be rather uniform by Rittel et al. [5, 6]. A deformed Nitinol specimen post-test is shown in Fig. 2, in which the shear-dominated nature of the gage deformation is clearly illustrated. Figure 2 shows a cropped portion of a larger 1,236×1,628 pixel image and is nominally 537×939 pixels.

Experiments

The shear compression specimens were deformed in uniaxial compression at room temperature using a computer-controlled servo-hydraulic loading frame (MTS model #358.10). Lubricant was applied between the specimen and compressive plates to minimize friction. Specimens were tested between a fixed bottom platen and a displacement-controlled top platen, with the top platen supported by pivots to minimize alignment issues. The specimens were tested at a nominal strain rate of 7×10^{-4} s^{-1} and imaged at 1.065 frames per second.

The deformation in the gage section of the specimen was characterized using digital image correlation (DIC). This is an *in-situ* optical correlation method used to measure

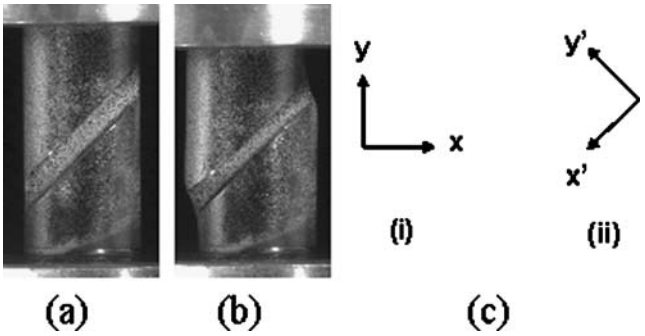

Fig. 2 SCS specimens of Nitinol: (**a**) before and (**b**) after deformation illustrating the shear-dominant nature of the deformation. The Cartesian axis x–y and the rotated (45° CCW) axis x'–y' are shown in (**c**)-(*i*) and (**c**)-(*ii*), respectively

displacements on the surface of an object by tracking a random pattern on the sample surface [7–10]. The random pattern can be inherent surface features or an artificially applied pattern, but must provide a sizeable number of correlation points at the magnification of imaging. In this experiment, the pattern was applied pre-test by first coating the sample in white paint and then spraying a light mist of black paint in a fine speckle pattern. Images were recorded using a 1,628×1,236 pixel Uniq UP-2000CL B/W digital CCD camera focused on the specimen surface and linked to a computer for data acquisition. A Nikon70–300 mm f/4.5–5.6G ED-IF AF-S VR Zoom Nikkor lens was utilized for zooming purposes. Since the deformation of interest was in the gage section and primarily in-plane, a single CCD camera could be used to capture the deformation. Images were taken after each displacement increment and post-processing was achieved with the software Vic-2D developed by Correlated Solutions [11] to extract the strain fields. Because the deformation was quite large, the strain distributions were computed in three groups and then superimposed in order to obtain the strain response for the entire experiment.

There are certain sources of error in these experiments that need to be briefly discussed. There exists friction between the compressive plates and the sample, although lubricant at these junctures helped to minimize this error. It may also be noted that frictional effects at the end-pieces of the SCS were found to be negligible as long as the specimen does not buckle [6]. There is grip alignment error, which was minimized by carefully aligning the grips and checking alignment with each experiment, and the self-aligning nature of the loading platen. There are also analysis errors due to any out-of-plane deformation of the specimen [5]. There are numerous parameters in the Vic-2D Correlated Solutions program that can be adjusted, and these parameters have a significant effect on the success of the computation. Improper lighting, dust, marks on the camera lens, inadequate camera shutter speed, or inadequate aperture can produce a faulty or blurred speckle pattern and cause failure. The accuracy of the correlation is also dependent on factors including but not limited to camera resolution, lens quality, marker resolution, degree of anisotropy, and degree of contrast. The camera resolution in this experiment was 54 pixels/mm. A significant source of error in correlation accuracy is electronic error, which was estimated by correlating a series of two images taken of the specimen under zero displacement and taking the maximum resultant error. In this experiment, the electronic error in the gage section was determined to be under 0.05%. An image intensity profile for the speckle pattern used in the following experiment is shown in Fig. 3, where the number of pixels at a greyscale intensity value ranging from 0 to 255 is plotted against that intensity value. The pattern is a bell-shaped distribution, indicating that adequate anisotropy and contrast necessary to ensure accurate results during correlation exists [12]. The subset size and the grid point spacing for this experiment were 21 pixels and one pixels respectively. A cubic b-spline interpolation for sub-pixel accuracy and an affine transformation for the subset shape function was used. The total error in the experiment, including that introduced by superposition of the correlations, is estimated to be ±0.25%.

Results

The primary goals of this work were to apply DIC to study the deformation mechanisms of Nitinol under large deformation shear loading and provide the first quantitative maps of the evolution of the full-field strain during this process. All strain maps (true strains outputted from DIC) and corresponding macroscopic stress–strain graphs are shown

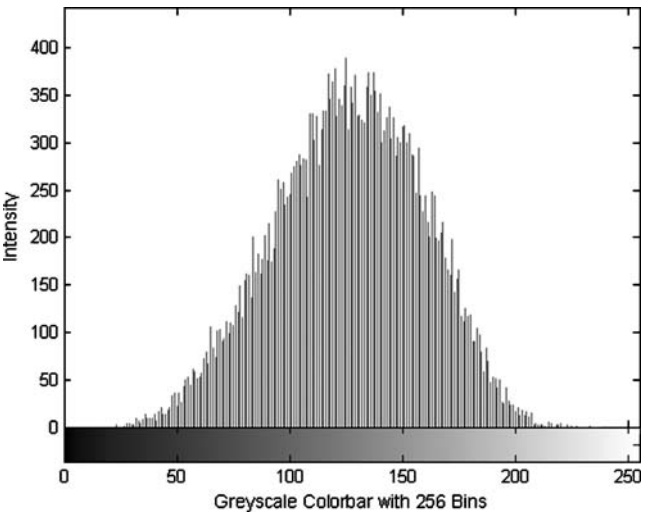

Fig. 3 Intensity histogram of the grey scale pattern used in the gage section of the shear compression specimen

in the material coordinate frame x'–y', rotated 45° counter-clockwise from the Cartesian (laboratory) x–y frame.

Figure 4 presents the macroscopic shear stress–shear strain behavior of the gage section of the shear compression specimen subjected to uniaxial compression under displacement control. The macroscopic shear strain is defined as the spatially averaged (in the gage section only) shear strain (ε_{xy}) obtained point-by-point from DIC, where the point-by-point strain components are rotated 45° CCW and presented in the x'–y' frame. The macroscopic shear stress is defined from the shear component of the axial load, measured from the load cell of the testing machine at the same instant of time when the DIC image was taken, and the shearing cross-sectional area. The plateau indicating the phase transformation from austenite to martensite is clearly discernable in the macroscopic stress–strain curve.

Note that at a particular stress value, the strain calculated by DIC will generally be slightly greater than the strain that one can calculate from the grip displacement data of the testing machine. This is due to the fact that the testing machine grip displacement data includes (1) strain induced in the cylindrical sections outside the gage section (albeit very small), (2) any adjustment of the grips, particularly at the beginning of the test, prior to making full contact with the specimen, and (3) errors inherent in the machine's collection of grip displacement data. In contrast to the strain data calculated from grip displacement, the spatially averaged DIC strain data is a strain measurement that is concentrated specifically on the area of interest (the gage section of the SCS specimen in this case) and has a high degree of spatial accuracy and resolution. These features are a compelling advantage of using DIC to spatially measure the local strain fields in order to determine constitutive material behavior.

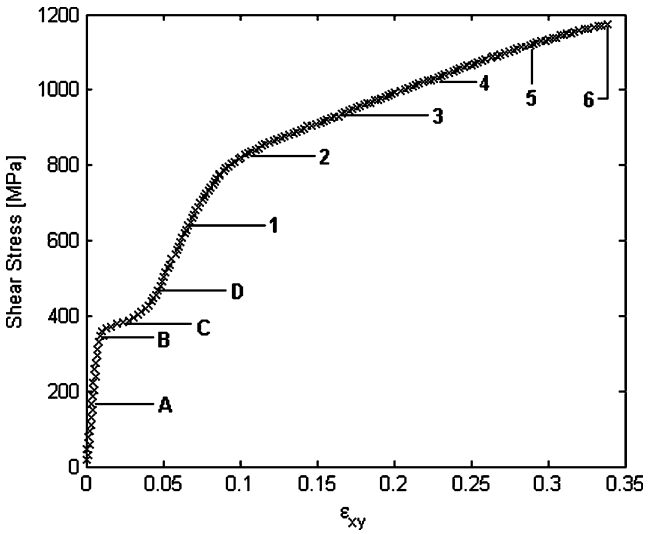

Fig. 4 The macroscopic shear stress–shear strain response in the gage section of a Nitinol SCS specimen. The macroscopic shear strain is defined as the spatially averaged shear strain (ε_{xy}) obtained point-by-point from DIC, where the point-by-point strains are rotated 45° CCW and presented in the x'–y' frame. The macroscopic shear stress is defined from the shear component of the axial load, measured from the load cell of the testing machine at the same instant of time when the DIC image was taken, and the shearing cross-sectional area

The points marked A–D and 1–6 in Fig. 4 represent different portions of the loading curve, which are distributed roughly as follows: (1) during the initial stages of the test (points A–B), the austenite is being elastically loaded, where B is just prior to the onset of transformation; (2) as the loading continues to increase, point C lies midway on the plateau of the curve, during phase transformation of austenite to martensite; (3) the phase transformation is macroscopically complete, and the martensite and residual austenite are being elastically loaded, at point D; and (4) at large strains, points 1–6 represent the plastic deformation of the transformed martensite and residual austenite.

Figures 5 and 9 show detailed progressions of the (rotated) strain field distribution (ε_{xx}, ε_{yy}, ε_{xy} in the x'–y' frame) at points A–D and 1–6 in Fig. 3. Figure 5 shows the full-field strain distribution for points A–D in Fig. 4, during the macroscopic phase transformation from austenite to martensite. Figure 9 details the strain distribution for points 1–6 in Fig. 4, after macroscopic transformation and during loading in the plastic regime. Note that the images in Fig. 5 and 9 had to be slightly cropped in post-processing. Specifically, 2.34 mm from the top of the specimen, 0.73 mm from the bottom of the specimen, 0.7235 from the left side of the specimen, and 0.7765 mm from the right side of the specimen have been trimmed, i.e. the specimen dimensions are 11.93×6.00 mm as indicated by the scale bars in Figs. 5 and 9. The area of high strain that appears at a 45° angle overlays with the slotted gage section cut out of the cylindrical specimen. The vertical crops only remove the top and bottom of the cylinders and have no effect on the gage area under examination. The horizontal crops result in a deletion of approximately 0.7 mm from each side of the gage section.

Details of the transformation prior to the onset of plasticity can be seen in Fig. 5. Figure 5 shows the strain maps presented in the rotated (45° CCW) coordinates x'–y' instead of the Cartesian (laboratory) components x–y. In this frame, the shear strain component dominates. Point A in Fig. 5 represents the strain state in the specimen before the deviation from linearity, when the specimen is still macroscopically in the austenitic state. Point B shows the strain near the onset of transformation. Point C represents a state midway through the superelastic plateau and the transformation from austenite to martensite. Point D represents the state when the specimen is nominally past the end of the transformation plateau and the martensite and residual austenite are being elastically loaded. While there is some strain concentration at the boundaries of the gage

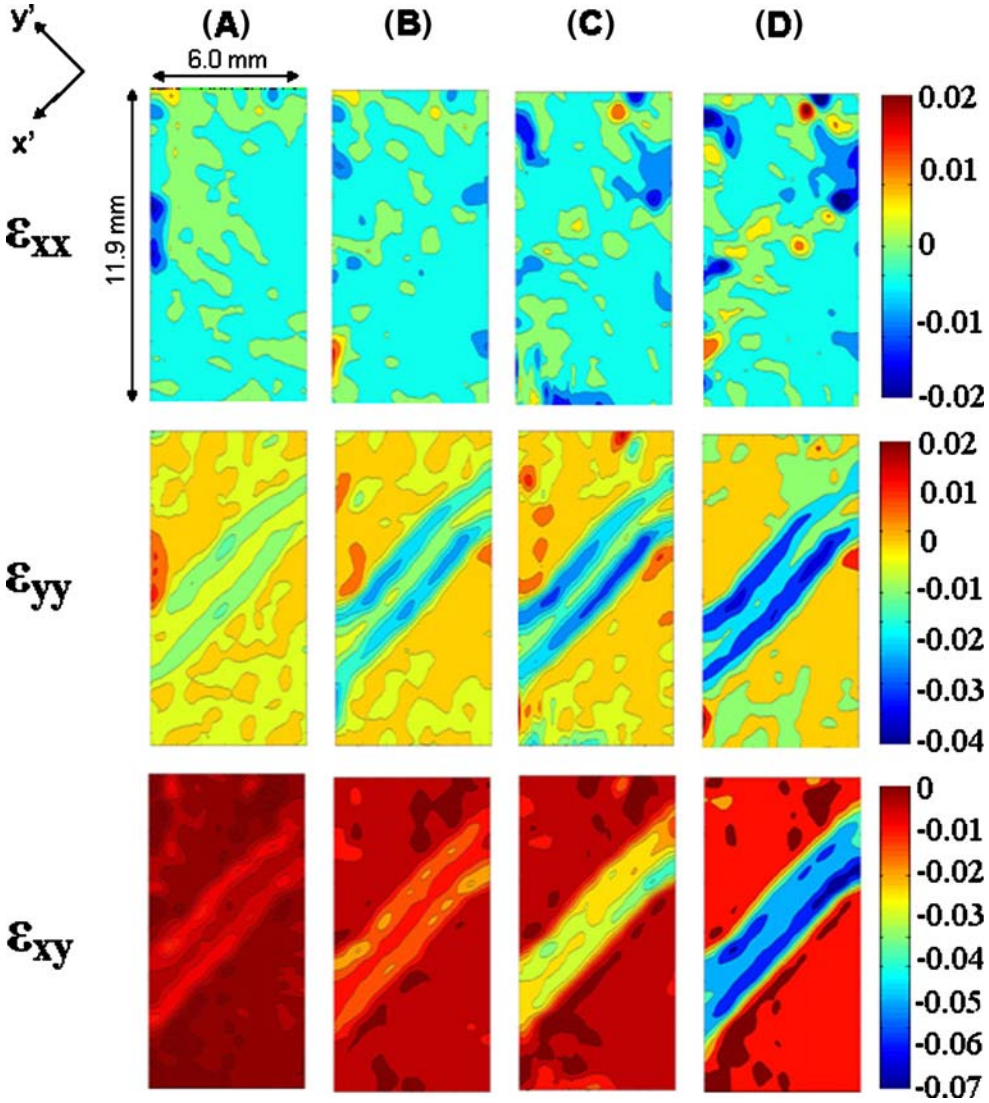

Fig. 5 The in-plane components of the strain field, rotated 45° CCW, obtained from DIC for the points A–D indicated in Fig. 4. These images detail phase transformation from austenite to martensite inside the gage section of the SCS and are at higher strain resolution than the images shown in Fig. 9

section due to edge effects of the loading, the strain is relatively homogenous in the gage section during phase transformation. At this spatial and temporal resolution, there is no evidence of the localized banding that has been extensively documented in strips of Nitinol under in uniaxial tension under a variety of testing conditions (see for example [13–17]). However, this may be a factor of the spatial resolution achieved in this experiment; there is a need for systematic studies at a range of strain rates and at higher temporal/spatial resolutions to conclusively determine the presence or absence of transformation in shear.

Figures 6, 7, and 8 show the strain profile plots during phase transformation from austenite to martensite inside the gage section of the SCS (points A–D in Fig. 4) for ε_{xx}, ε_{yy},

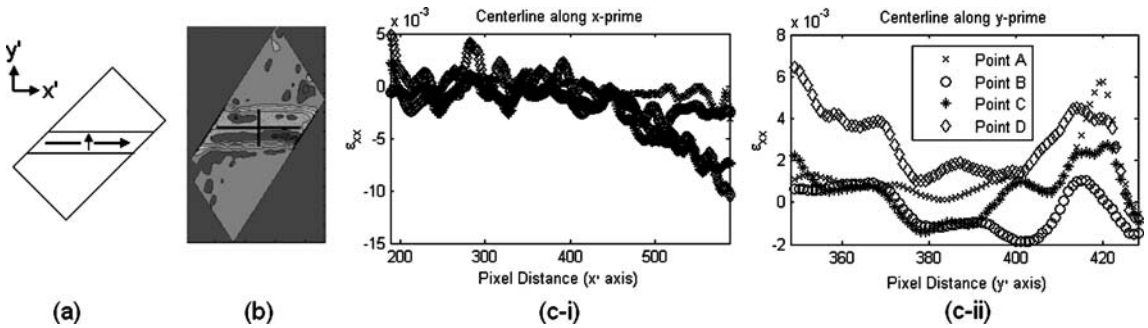

Fig. 6 Strain (ε_{xx}) profile plots for points A–D in Fig. 4, where the strain components are given in the x'–y' frame (rotated 45° CCW from x–y)

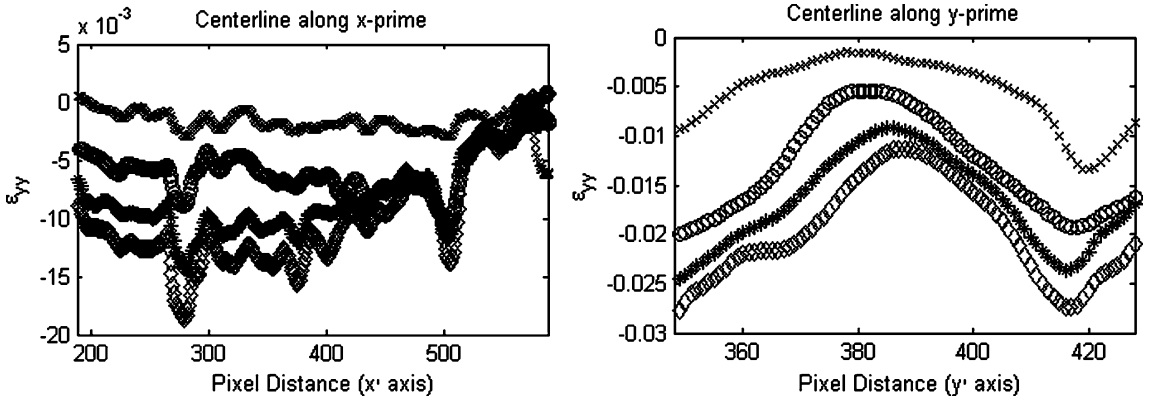

Fig. 7 Strain (ε_{yy}) profile plots for points A–D in Fig. 4, where the strain components are given in the x'–y' frame (rotated 45° CCW from x–y)

and ε_{xy}, respectively. The strain components are given in the x'–y' frame, rotated 45° CCW from the laboratory (x–y) frame. Figure 6(a) is a schematic of the specimen rotated 45° counterclockwise. The strain profiles are taken along the x' and y' axes, which are now horizontal and vertical lines, in the directions shown by the arrows in Fig. 6(a). In Fig. 6(b), the exact length of the strain profiles in the x' and y' directions are superimposed as horizontal and vertical lines, respectively, on a rotated specimen. Figure 6(c-i) shows the strain profile along the x'–axis in the gage section for points A–D. Figure 6(c-ii) shows the strain profile along the y'–axis in the gage section for points A–D. The legend for all strain profile plots in Figs. 6–8 is shown in Fig. 6(c-ii). Strain profiles for the ε_{yy} and ε_{xy} components are shown in Figs. 7 and 8. Edge effects of loading are visible at the ends of the y'-axis profile, particularly the ε_{yy} strain profile.

Details of the strain field in the entire SCS specimen at large strains past the superelastic region, corresponding to points 1–6 in Fig. 4, are shown in Fig. 9. Figure 9 shows the strain maps presented in the rotated (45° counterclockwise) coordinates x'–y' instead of the laboratory components x–y. In this frame, the shear strain component dominates. As the loading continues, the level of strain continues to increase throughout the gage section, which is now fully martensite and residual austenite. At point 1, the strain is still relatively homogenous inside the gage section, with the exception of some localized strain as a result of boundary effects on the edges of the gage section. At points 2–6, the strain in the middle of the gage section starts to grow and the strain field itself becomes less homogeneous. Particularly in points 4–6, there is an appearance of 'patchiness' of the strain and a much higher degree of inhomogeneity in the middle of the gage section. Although there is a large amount of deformation being applied to the cylinder, the high strain regions do occur only inside of the gage section, as expected. At the end of the test (point 6 in Figs. 4 and 9), ε_{yy} inside the gage section is on the order of 0.2, ε_{xx} is on the order of 0.1, and ε_{xy} is on the order of 0.5, but outside of the gage section the strain remains relatively small and homogenous, in accord with the basic characteristic of the SCS.

Figure 10 shows the development of strain (ε_{xx}, ε_{yy}, and ε_{xy}) profiles for points A–D and 1–6, following along the x' and y' axes exactly as indicated in Fig. 6(a) and (b) and taken at every third point. The strain components are given in the x'–y' frame, rotated 45° CCW from the laboratory (x–y) frame. In Fig. 10, the development of

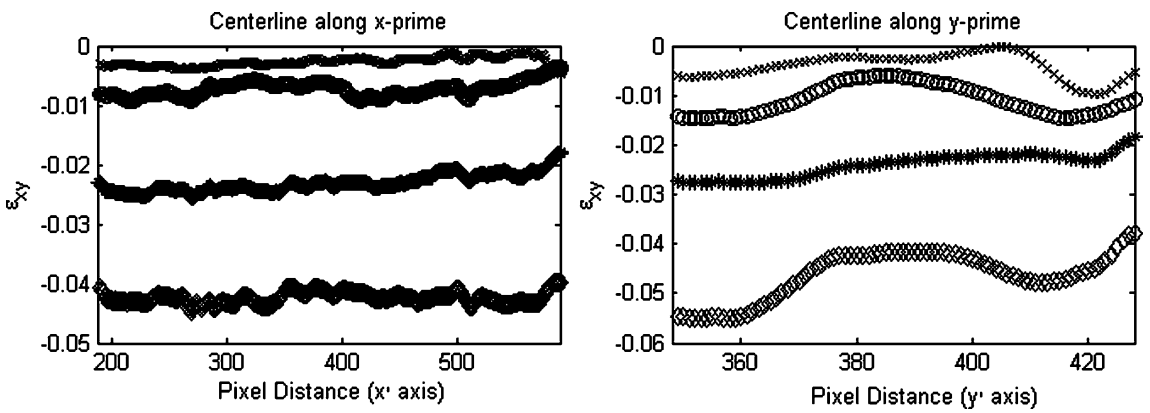

Fig. 8 Strain (ε_{xy}) profile plots for points A–D in Fig. 4, where the strain components are given in the x'–y' frame (rotated 45° CCW from x–y)

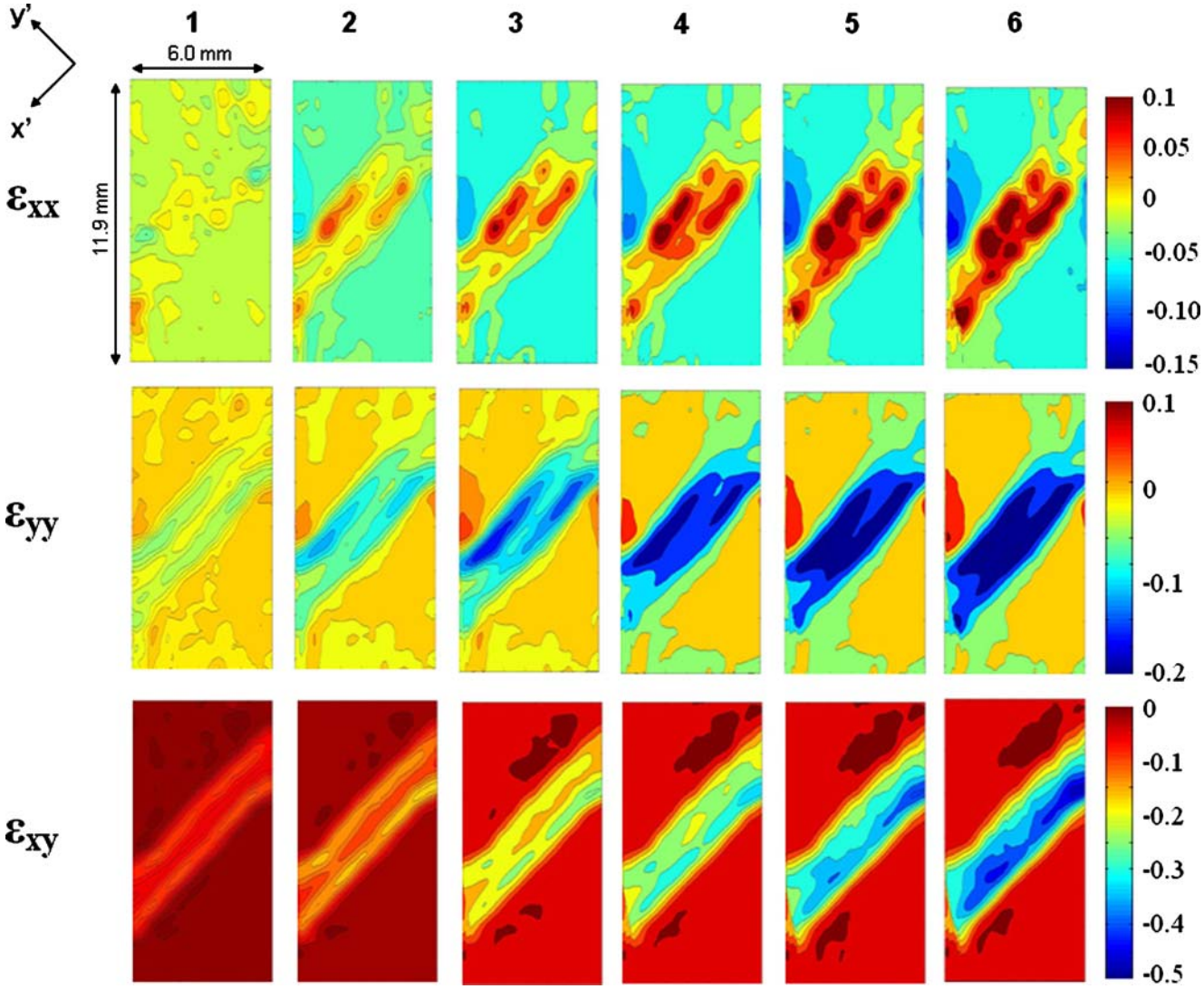

Fig. 9 The in-plane components of the strain field, rotated 45° CCW, obtained from DIC for the points 1–6 indicated in Fig. 4. These images detail strains inside the gage section during the onset and development of plastic deformation beyond the superelastic plateau

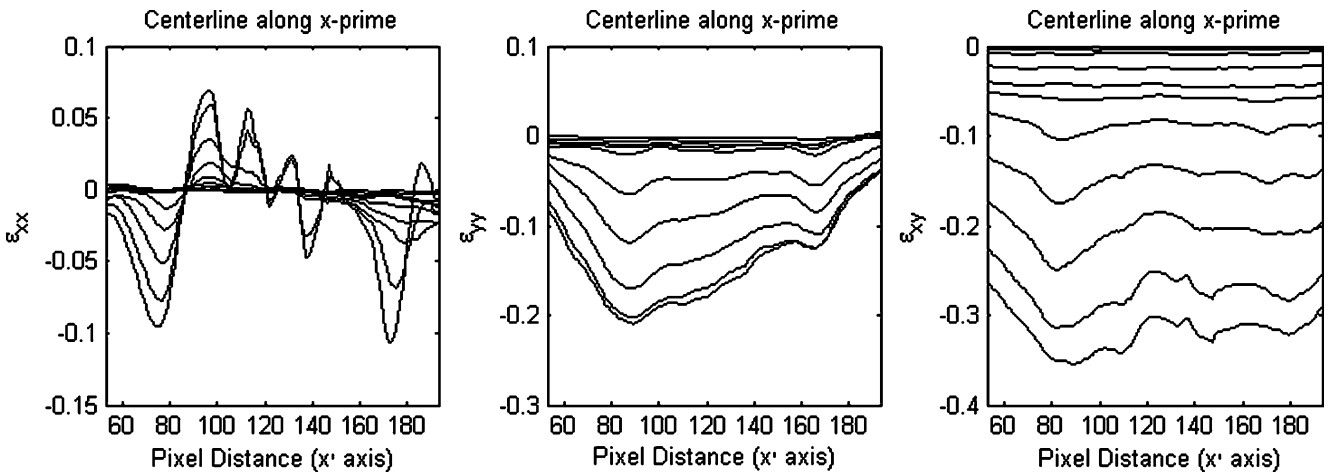

Fig. 10 Strain (ε_{xx}, ε_{yy}, and ε_{xy}) profile plots for points A–D and points 1–6 in Fig. 4, where the strain components are given in the x'–y' frame (rotated 45° CCW from x–y)

anisotropy in the gage section in the plastic regime (points 1–6) is evident in all strain components ε_{xx}, ε_{yy}, and ε_{xy}, particularly in ε_{xx}.

Discussion

The combination of the shear compression specimen (SCS) geometry and digital image correlation (DIC) has been successfully used to produce relatively uniform states of stress and strain in Nitinol under large deformation shear dominant loading. The use of this specimen enabled the investigation of the behavior of Nitinol under large shear loading during plastic deformation of the martensite and residual austenite.

The experimental observations presented in the previous section provide various insights into the mechanism of deformation in initially austenitic Nitinol under shear-dominant loading. Tension–torsion tests on Nitinol performed by McNaney et al. showed significantly different characteristics depending on the loading path, indicating that shear deformation may inhibit the development of localized deformation during martensitic transformation [18]. The results of the present study also suggest that it may be possible to inhibit localization during phase transformation in Nitinol under shear dominant loading conditions versus uniaxial tension, and provide an experimental methodology that can be used to systematically probe this hypothesis in a variety of testing conditions.

Although there are localized regions of higher strain on the boundaries of the gage section, at this spatial and temporal resolution the deformation is relatively homogenous in the middle of the gage during the region of phase transformation indicated in the macroscopic shear stress–shear strain behavior. However, deformation inside the gage section becomes less homogenous during plastic deformation. At points 1–6 in Fig. 4, the appearance and development of inhomogeneous regions of strain can be seen in the center of the gage section (Fig. 9). The reason for the development of inhomogeneity during plastic deformation may be attributed to the anisotropy that the phase transformation introduces in the material. The plastic deformation of Nitinol under large shear also exhibits relatively low hardening.

Conclusions

Digital image correlation (DIC) has been used in conjunction with the shear compression specimen (SCS) to study the quantitative full-field strain fields of a shape memory alloy (Nitinol) subjected to large-scale shear deformation. The main results of the study can be summarized as follows,

1. Shear deformation of Nitinol appears to be relatively homogenous during phase transformation (visible macroscopically in Fig. 4) at the spatial and temporal resolution in this experiment, indicating that shear dominant deformation may impede the development of localized bands of deformation during phase transformation in Nitinol. This is in contrast to the clearly visible inhomogeneous (localized) nature of deformation observed during phase transformation in uniaxial tension [13–17]. There is a need for further systematic experimentation at various spatial and temporal resolutions to validate the absence or existence of phase transformation in this shear-dominant mode.
2. Plastic deformation of Nitinol is not homogeneous during large-scale shear loading. In the plastic regime of the SCS gage section, as defined by the macroscopic shear stress–shear strain data shown in Fig. 4, there are visible patches of localized strain (Fig. 9). This may be due to the introduction of additional inhomogeneity as a result of phase transformation, where the high strain regions visible inside the gage section are due to the non-uniformity of the martensite and residual untransformed austenite. The development of inhomogeneity can also be seen clearly in the strain profiles shown in Fig. 10.
3. The macroscopic stress–strain behavior of Nitinol under large shear deformation does not indicate a significant amount of strain hardening during plasticity.

Acknowledgements We gratefully acknowledge the support of the Army Research Office (W911NF-04-1-0156), the National Science Foundation (DMS-0311788) and the Powell foundation. We thank Correlated Solutions, Inc. for providing the DIC correlation software used in these experiments.

References

1. Otsuka K, Wayman CM (1998) Mechanism of the shape memory effect and superelasticity. In: Otsuka K, Wayman CM (eds) Shape memory materials. Cambridge University Press, Cambridge
2. Bhattacharya K (2004) Microstructure of Martensite: Why it forms and how it gives rise to the shape-memory effect. Oxford University Press, Oxford
3. Sehitoglu H, Jun J, Zhang X, Karaman I, Chumlyakov Y, Maier HJ et al (2001) Shape memory and pseudoelastic behavior of 51.5% Ni–Ti single crystals in solutionized and overaged state. Acta Mater 4917:3609–3620 doi:10.1016/S1359-6454(01)00216-6
4. Pelton A, Duerig T, Steckel D (2004) A guide to shape memory and superelasticity in nitinol medical devices. Minim Invasive Ther Allied Technol 13:218–221 doi:10.1080/13645700410017236
5. Rittel D, Lee S, Ravichandran G (2002) A shear-compression specimen for large strain testing. Exp Mech 421:58–64 doi:10.1007/BF02411052

6. Dorogoy A, Rittel D (2005) Numerical validation of the shear compression specimen (SCS). Part I: quasi-static large strain testing. Exp Mech 42:167–177 doi:10.1007/BF02428190
7. Bruck HA, McNeill SR, Sutton MA, Peters WH (1989) Digital image correlation using Newton–Raphson method of partial–differential correction. Exp Mech 293:261–267 doi:10.1007/BF02321405
8. Cheng P, Sutton MA, Schreier HW, McNeill SR (2002) Full-field speckle pattern image correlation with B-spline deformation function. Exp Mech 423:344–352 doi:10.1007/BF02410992
9. Chu TC, Ranson WF, Sutton MA, Peters WH (1985) Applications of digital image correlation techniques to experimental mechanics. Exp Mech 253:232–244 doi:10.1007/BF02325092
10. Schreier HW, Sutton MA (2002) Systematic errors in digital image correlation due to undermatched subset shape functions. Exp Mech 423:303–310 doi:10.1007/BF02410987
11. Correlated Solutions.West Columbia, South Carolina, www.correlatedsolutions.com
12. Berfield TA, Patel JK, Shimmin RG, Braun PV, Lambros J, Sottos NR (2007) Micro- and nanoscale deformation measurement of surface and internal planes via digital image correlation. Exp Mech 47:51–62 doi:10.1007/s11340-006-0531-2
13. Daly S, Ravichandran G, Bhattacharya K (2007) Stress-induced martensitic transformation in thin sheets of nitinol. Acta Mater 55:3593–3600 doi:10.1016/j.actamat.2007.02.011
14. Shaw JA, Kyriakides S (1997) On the nucleation and propagation of phase transformation fronts in a NiTi alloy. Acta Metall 452:683–700
15. Pieczyska EA, Gadaj SP, Nowacki WK, Tobushi H (2004) Thermomechanical investigations of martensitic and reverse transformations in TiNi shape memory alloy. Bull Pol Acad Sci Tech Sci 523:165–171
16. Schmahl WW, Khalil-Allafi J, Hasse B, Wagner M, Heckmann A, Somsen C (2004) Investigation of the phase evolution in a superelastic NiTi shape memory alloy (50.7 at.% Ni) under extensional load with synchrotron radiation. Mater Sci Eng A 3781–2:81–85 doi:10.1016/j.msea.2003.11.081
17. Shaw JA, Kyriakides S (1997) Initiation and propagation of localized deformation in elasto-plastic strips under uniaxial tension. Int J Plast 1310:837–871 doi:10.1016/S0749-6419(97)00062-4
18. McNaney JM, Imbeni V, Jung Y, Papadopoulos P, Ritchie RO (2003) An experimental study of the superelastic effect in a shape-memory Nitinol alloy under biaxial loading. Mech Mater 3510:969–986 doi:10.1016/S0167-6636(02)00310-1